Spatial Mode Selection in a Passively Coupled Fiber Laser: Theory and Experiment

A THESIS
SUBMITTED TO THE FACULTY OF THE GRADUATE SCHOOL
OF THE UNIVERSITY OF MINNESOTA
BY

Erik Lee Tilseth

IN PARTIAL FULFILLMENT OF THE REQUIREMENTS
FOR THE DEGREE OF
MASTER OF SCIENCE

James R. Leger, advisor

September, 2019

Acknowledgements

I would like to begin by thanking my advisor, Prof. Jim Leger for supporting this research. Thanks also to Profs. Taner Akkin and Joey Talghader for reviewing my thesis. A big thank you goes to Johan Nilsson, Jonathan Price, Jayanta Sahu and the rest of the team at the University of Southampton's Optoelectronics Research Centre for collaboration and fabricating the custom optical fiber used in these experiments.

Acknowledgements also go to Hung-Sheng Chiang for helping me out in the early days of my research, Mint Kunkel for providing helpful feedback on this work, and Nathan Mowry for providing a measurement of the passive fiber absorption necessary for my theoretical model.

I would also like to thank my family and friends for their support during the last few years.

Abstract

In this thesis, self-phasing due to spatial mode selection in a two-element passively coupled fiber laser is studied. The fields emitted by a two-core ytterbium doped fiber are coherently combined with a Dammann grating in an external cavity. We measure the combined beam power and supermode relative phase in the presence of phase errors between the gain elements and find that implementation of spatial mode selection via beam recycling results in a 90% increase in the average output power and nearly $\pi/2$ radians of passive phase adjustment. We show that these results require a phase of zero (modulo 2π) between the beams in the external cavity. Otherwise, the average output power and the coherence of the laser decreases. These findings are supported by the results of an eigenmode analysis of the resonator. These results show that beam recycling is a useful resonator design feature but must be appropriately implemented to obtain beneficial results.

Contents

List of Figures

Chapter 1

Introduction

Passive coherent beam combination (CBC) provides a possible path towards scaling laser radiance beyond what can be obtained from a single oscillator. Passive systems are attractive compared to active CBC systems in that they do not require complicated control electronics to establish and maintain phase control between gain elements. Instead, phase control is maintained by the system itself with the assistance of various self-phasing mechanisms. Deeper study of these self-phasing mechanisms leads to methods for engineering these systems to obtain the best possible performance.

This thesis addresses self-phasing due to spatial mode effects in a passively coupled fiber laser. In Chapter 2, we provide background on coherent beam combining (CBC) systems. This includes a discussion of different types of coupled laser cavities and the self-phasing effects that occur in passive CBC systems. We describe beam recycling, which is a resonator design feature that leads to spatial mode selection.

In Chapter 3, we analyze the Dammann grating and show that it can combine two beams into one and vice versa, forming the basis of a passively coupled resonator. Then, we perform an eigenmode analysis of the Dammann grating resonator and show that spatial mode selection results in improved performance in the presence of induced phase errors between the gain elements. We also find the particular conditions required to achieve spatial mode selection.

Chapter 4 discusses an experimental setup using a two-core ytterbium doped gain fiber to test the predictions made by theory. We show data for the combined beam power and supermode phase and demonstrate what happens when beam recycling is

not properly implemented.

We conclude in Chapter 5 with a summary of results and suggestions for future work on this subject.

Chapter 2

Background on Coherent Beam Combination

In this chapter, we provide an introduction to coherent beam combination (CBC). We start by describing the goals of beam combining systems, which can be classified as either coherent or incoherent. Then, we mention some methods to produce a CBC resonator and move on to a description of active and passive (self-phasing) CBC systems. Following this, we describe several self-phasing effects that are present in passive CBC resonators. We conclude with a discussion of spatial mode selection, the particular self-phasing effect that is of interest in this thesis.

In a single laser oscillator, there is a limit to the amount of power that can be extracted from the system. Pumping the gain medium at very high levels can induce thermal distortions of the beam and cause damage to the laser. The goal of a beam combining system is to overcome these limitations by using several low-power gain elements whose outputs are combined into a single high-power output beam. Such a system can increase both the power and radiance emitted by a single laser aperture to levels higher than can be achieved using a single gain medium [1]. Beam combining can be implemented in either a coherent system, where the electric fields emitted by the gain elements are added together, or in an incoherent system, where the powers emitted by the gain elements are added together. An example of incoherent beam combining is wavelength beam combining. In this case, each gain element operates at a slightly

different wavelength and a dispersive element, such as a grating or prism, combines the beams from each element inside an external cavity. One such method combined 5 ytterbium fiber lasers with a resulting beam quality similar to that of a single fiber [2].

In contrast, a coherent beam combining (CBC) system has gain elements operating at the same wavelength, and the combined beam is a sum of electric fields from the gain elements. Several methods have been explored to combine beams in a coherent manner, and the method we will focus on involves coupled cavities. Some coupled cavities, including the Michelson resonator [3] and Dammann grating resonator [4], are referred to as superposition architectures, shown in Figure 2.1a. Other coupled cavities, such as the Talbot cavity [5], spatially filtered cavity [6], and evanescently coupled cavity [7], are called parallel coupled architectures, shown in Figure 2.1b. Part of achieving coherent beam combination is establishing and maintaining phase control between the gain elements. This can be done using electronic control systems, as in active CBC, or done by the array itself, as in passive CBC.

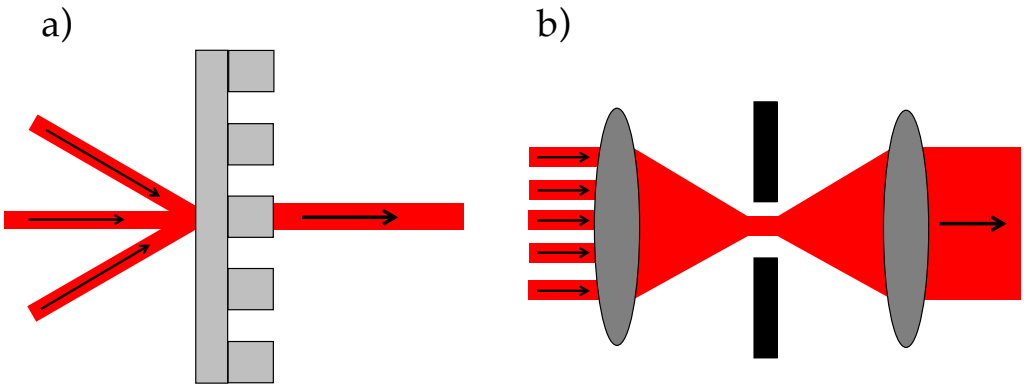

Figure 2.1: Example of superposition architecture using a Dammann grating (a) and example of a parallel coupling architecture using spatial filtering (b).

Active CBC systems utilize control electronics to provide phase control of the gain elements. A feedback loop samples the signals emitted by the gain elements and uses control algorithms to modify the phases of the gain elements. These algorithms are intended to maintain the desired output power and beam quality emitted by the array. One example of an active CBC system is based on optical heterodyne detection [8, 9]. These systems form heterodyne signals by mixing a portion of each gain element's output

with a reference. As a result, an array of N elements requires N detectors to provide phase locking and adjustment for each element. A second example, LOCSET, does not require beating each array element with a reference [10]. As a result, only one detector is needed to control the phase locking. At least nine fiber amplifiers have been combined in this manner, and it has been suggested that this technique is scalable to 100 elements [11]. A third example is a system using hill-climbing algorithms based on the stochastic parallel gradient descent (SPGD) algorithm [12, 13]. Since the rise time of the SPGD phase control is proportional to the number of gain elements [14], it is difficult to scale this method to large arrays.

In contrast, passive CBC systems do not utilize control electronics. This results in a simpler system as a whole. Recently, a large amount of work has used doped fibers for gain media due to properties such as their resilience to thermal-induced mode distortions and the availability of high gains [15]. Passive coupling has been successfully applied to arrays with at least 20 fibers [16]. Several properties of these systems have been studied such as the cophasing dynamics and response time to perturbations [17, 18] and the effect of quantum noise on phase locking [19]. Experiments have also shown the possibility of passive CBC for Q-switched systems [20] and mode-locked systems [21].

Passive CBC systems have shown success, but it is unclear exactly why these systems are successful and what influences their behavior. In addition, the limits of passive CBC are not known. Many physical mechanisms influence passive self-phasing, and careful study of these mechanisms gives insight into how to engineer the beam combining systems to achieve beneficial performance. We now briefly describe some of these effects.

Wavelength tuning, or longitudinal mode selection, is a significant effect in a system that contains fibers of different lengths or a wide oscillation bandwidth. Two coupled resonators with lengths L_1 and L_2 each have longitudinal modes separated by $\Delta\nu_{1,2} = c/(2nL_{1,2})$. The system oscillates in a longitudinal mode that is shared by each resonator, as seen in Figure 2.2. A phase error introduced to one of the oscillators causes the modes to shift laterally. A shared mode can then be found at a different wavelength to compensate for the phase error. This tuning ability is decreased by a narrow gain bandwidth or nearly identical resonator lengths. Wavelength tuning poses limitations on the array size since the probability of having common longitudinal modes decreases as the number of gain elements increases. As a result, several models have

shown that arrays that implement only this self-phasing mechanism suffer a reduced combining efficiency if the number of elements is greater than 8 [22, 23, 24].

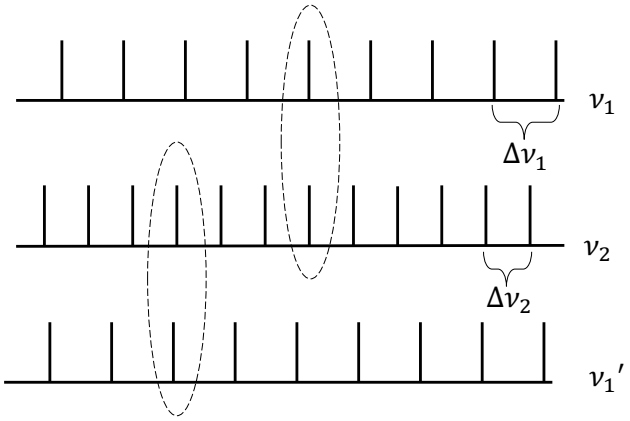

Figure 2.2: Description of wavelength tuning. ν_1' represents the ν_1 modes after an induced phase error. Common longitudinal modes are circled.

The heating of fiber cores, often due to pump lasers, is known to cause thermal-induced index changes [25, 26]. Non-radiative relaxation processes of the fiber dopant cause some of the pump power to be converted into heat [27]. This can cause index changes and thus phase changes in signals propagating in the core. For example, in a 10W ytterbium fiber amplifier, a phase shift of 2000 waves occurred during the first 8 minutes of operation, which corresponds to a 10°C increase in the fiber temperature [28]. A CBC system with gain elements in different thermal environments is thus susceptible to significant phase errors. Thermal effects can be mitigated by keeping the gain elements in a common thermal environment, such as in a twin-core fiber [27].

The nonresonant nonlinearity, or Kerr effect, of the gain media is relevant in any high-power CBC system. The high intensity of the laser signal can itself modify the refractive index of the gain media or waveguide. This change can be expressed as $\Delta n = n_2 I$, where I is the intensity of the circulating field. For a silica fiber, $n_2 = 3 \times 10^{-20}\text{m}^2/\text{W}$ [29]. For a fiber with core area A and length L containing power $P(x)$ at position x, one can compute the accumulated phase using $\phi_{Kerr} = \frac{2\pi}{\lambda A}\int_0^L n_2 P(x)\, dx$. For example, using $\lambda = 1$ micron, $L = 10$ meters, a constant power of 10 watts, and a

core diameter of 4 microns results in a phase shift of 1.5 rad, and even smaller phase shifts could have a significant effect on a CBC system. The Kerr effect has been discussed in various models and may cause improved resonator performance [23, 30, 31], but can also cause Q-switching instabilities to occur [32].

The Kramers-Kronig (KK) effect, or resonant nonlinearity, arises from differences in electronic state populations in an active medium. The population difference, or gain, that is induced by a pump signal changes the refractive index of the medium [33]. The gain and resulting phase shift are related by Henry's α-parameter [34]. In an experiment using ytterbium-doped fiber, a π radian phase shift at 1550nm occurred for only 14mW of pump power at 980nm [35]. In a CBC system, the KK effect is relevant when there is a difference in gain between elements. In a two element fiber laser, the KK effect partially compensated for phase errors between gain elements, but did not appear to be beneficial for power scaling [36]. Subsequent numerical simulations indicated that this effect also did not improve performance for larger arrays [37]. The KK effect can cause other laser behaviors, such as hysteresis and bistability, to occur [38].

Regenerative feedback occurs when gain media experience their own feedback sources in addition to the feedback applied to the entire array. One model predicts that a coherent array incorporating regenerative feedback and the KK effect operates in a way that compensates for random differences in fiber lengths [39]. Another theory [40] predicted that in the absence of nonlinearities, application of regenerative feedback to all elements in a coherently coupled array resulted in improved coherence. Experiments are still needed to determine the validity of these models.

The self-phasing mechanism we address in this thesis is spatial mode selection. This effect occurs when gain clamping selects the coupled-resonator supermode with the lowest loss for oscillation. This effect has been analyzed in a Michelson resonator [41], which found that adding a fourth mirror results in a system whose combined beam power and supermode phase state are less sensitive to phase errors between the gain elements. The resulting generalized Michelson resonator, shown in Figure 2.3a, has been described as implementing "beam recycling" since the fourth mirror (shown in red) causes the resonator to recycle energy that would otherwise be lost from the resonator. However, the phases between the output and recycling arms must be matched for spatial mode selection to work properly. These predictions were experimentally demonstrated

in a polarization-multiplexed laser with a single Nd:YAG gain medium [42]. While it validates the theory, it does not represent a true beam combining system with separate array elements. More recently, Monte Carlo simulations showed that the average output power from a beam recycling resonator scales with the number of gain elements [43]. However, the scaling occurs only for particular resonator architectures.

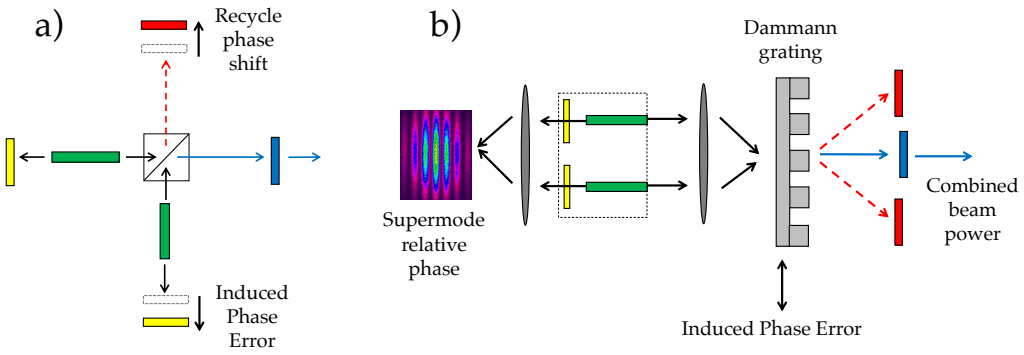

Figure 2.3: Concept of beam recycling in a Michelson resonator (a) and Dammann grating resonator (b).

In this thesis, we present an analysis and experimental demonstration of spatial mode selection in a Dammann grating resonator, shown in Figure 2.3b. The Dammann grating combines the beams from two gain media into a combined beam (in blue) and also produces two uncombined beams (in red). Optical feedback applied to the combined beam results in a "standard resonator", and the addition of feedback to the uncombined beams results in a "recycling resonator". The recycle mirror in the Michelson resonator is analogous to the red feedback mirrors shown in Figure 2.3b. In Chapter 3, we describe the behavior of the Dammann grating and show how it can combine beams in a resonator. In addition, we apply eigenmode analysis and a gain saturation model to both the standard and recycling resonators to compute the supermode relative phase and combined beam power versus induced phase errors between the gain

elements. In Chapter 4, we discuss an experimental Dammann resonator containing a two-core ytterbium-doped fiber and discuss the various ways we reduce other self-phasing effects. We then present data for the standard and recycling resonators and discuss how they compare to theory. Chapter 5 concludes the thesis by reviewing the results and providing suggestions for future work.

Chapter 3

Analysis of a Dammann Grating Resonator

The previous chapter gave an introduction to the field of coherent beam combination and ended with a brief description of the work addressed in this thesis. In this chapter, we analyze the behavior of a Dammann grating resonator containing two gain media. Our goal is to find how the oscillating supermode phase and combined beam power vary with respect to induced phase errors between the gain elements. First, we analyze the Dammann grating and show how it can be used to form a passively coupled resonator. Then, we apply eigenmode analysis with a gain saturation model to both the standard and recycling resonators and compare their properties.

3.1 Dammann Grating

In this section, we describe a model of the Dammann grating and demonstrate how it can be used to perform beam combination inside of a laser resonator. In particular, we show it can couple energy from one beam into two and vice versa. We will derive a matrix to illustrate its action on fields inside the resonator which are represented as vectors.

A general Dammann grating has a complex periodic structure and couples light into N diffraction orders of equal intensity [44]. In this work, we use the simplest type of Dammann grating (N=2), which is a 50% duty cycle square wave phase grating with

a phase depth of π radians, transmittance $t_A(x)$, and spatial period d (or fundamental frequency $f_0 = \frac{1}{d}$). The angular plane wave spectrum (APWS) of the grating is, using Problem 4-14 of [45],

$$T_A(f_x) = \mathcal{F}\{t_A(x)\} = \delta(f_x) - \sum_{n=-\infty}^{\infty} \text{sinc}\left(\frac{n}{2}\right) \delta(f_x - nf_0) \tag{3.1}$$

where $\text{sinc}(x) \equiv \sin(\pi x)/\pi x$ and $\mathcal{F}\{\cdot\}$ denotes the Fourier transform. The grating spectrum consists of plane wave components at frequencies nf_0. Since $\text{sinc}(x)$ is zero for integer x, only terms of odd n have nonzero amplitudes. If we include spatial translation of the grating by x_0, the APWS becomes, by the Fourier shift theorem [45],

$$\widetilde{T}_A(f_x) = \mathcal{F}\{t_A(x - x_0)\} = \exp(-i2\pi f_x x_0) T_A(f_x) \tag{3.2}$$

$$= \delta(f_x) - \sum_{n=-\infty}^{\infty} \text{sinc}\left(\frac{n}{2}\right) \delta(f_x - nf_0) \exp(-i\phi_n) \tag{3.3}$$

The result of translation is that the component at frequency nf_0 acquires a phase shift $\phi_n = 2\pi n f_0 x_0$.

In general, a field of wavelength λ incident on the grating with APWS $E_i(f_x)$ will result in an output field with APWS $\widetilde{T}_A(f_x) * E_i(f_x)$, where $*$ denotes convolution. If the incident field is an on-axis plane wave, the output field spectrum is simply $\widetilde{T}_A(f_x)$. This scenario is shown in Figure 3.1a. In this case, one can show using Equation (3.3) that 40.5% of the incident power is coupled into both the f_0 and $-f_0$ components of the output. Using the conversion $f_x = \sin\theta/\lambda$, these plane wave components propagate at angles $\theta = \pm\lambda f_0$, where we have used a small angle approximation. A lens of focal length f can focus these components on the back focal plane at spatial coordinates $x = \pm f\lambda f_0$. If gain media are placed at these locations, the Dammann grating and lens acting together can couple a single incident beam into two gain media and form the basis of a Dammann grating resonator.

In addition, due to the translation, we can define the phase shift between these components as

$$\Delta\phi = \phi_1 - \phi_{-1} = 4\pi f_0 x_0 = \frac{4\pi x_0}{d} \tag{3.4}$$

This represents the induced phase error between gain elements, a variable of interest throughout this work.

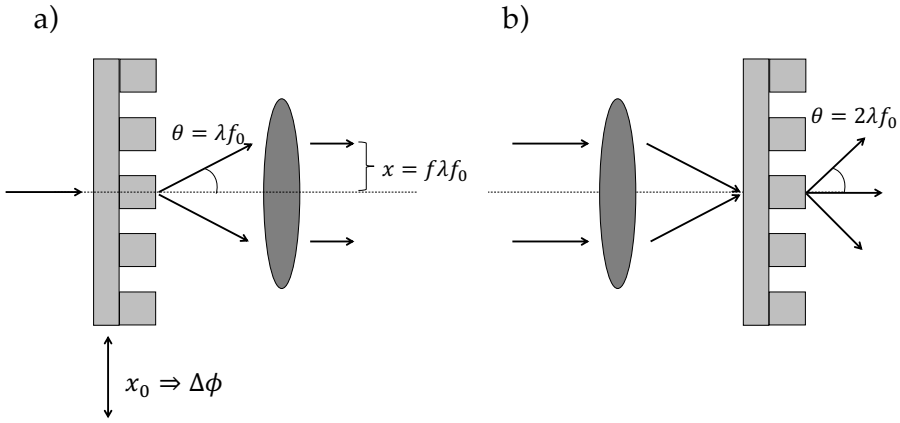

Figure 3.1: Action of the Dammann grating on beams incident at $\theta = 0$ (a) and $\theta = \pm\lambda f_0$ (b). The lens has focal length f.

Now consider beams emitted by the gain media that are incident on the Dammann grating at angles $\theta = \pm\lambda f_0$, as shown in Figure 3.1b. One can show the output field has components that propagate at $\theta = 0$ and $\theta = \pm 2\lambda f_0$ and that both incident components contribute equal amplitudes to the $\theta = 0$ component of the output field. The $\theta = 0$ component represents the combined beam inside the laser resonator.

From the two cases, we see there are five propagation angles of interest in this resonator. Round-trip analysis of a resonator requires us to account for the amplitudes and phases of the five components as they propagate through the resonator. This information can be collected in a 5x1 vector $\mathbf{U}$ given by

$$\mathbf{U} = \begin{bmatrix} U_2 \\ U_1 \\ U_0 \\ U_{-1} \\ U_{-2} \end{bmatrix} \tag{3.5}$$

where U_j is the amplitude and phase of the component propagating at the angle $\theta = j\lambda f_0$. In addition, the resonator elements that act on the field distribution $\mathbf{U}$ can be described as 5x5 matrices. These matrices indicate how the amplitude and phase of

the propagation components change due to a specific element. To form the Dammann grating matrix $\mathbf{D}$, we first truncate Equation (3.3) to obtain a form that contains only the first and third harmonics of the grating,

$$\widetilde{T}_A(f_x) \approx \sum_{n=-4}^{4} c_n \delta(f_x - nf_0) \tag{3.6}$$

where the coefficients are

$$c_n = \begin{cases} 0, & \text{if } n \text{ even} \\ \frac{2}{\pi}\exp\left(\frac{-in\Delta\phi}{2}\right), & n = -1, 1 \\ -\frac{2}{3\pi}\exp\left(\frac{-in\Delta\phi}{2}\right), & n = -3, 3 \end{cases} \tag{3.7}$$

Then, we collect the coefficients into a matix as

$$\mathbf{D} = \begin{bmatrix} c_0 & c_{-1} & c_{-2} & c_{-3} & c_{-4} \\ c_1 & c_0 & c_{-1} & c_{-2} & c_{-3} \\ c_2 & c_1 & c_0 & c_{-1} & c_{-2} \\ c_3 & c_2 & c_1 & c_0 & c_{-1} \\ c_4 & c_3 & c_2 & c_1 & c_0 \end{bmatrix} \tag{3.8}$$

For example, the result of a unit amplitude on-axis plane wave incident on the grating is

$$\mathbf{D}\begin{bmatrix} 0 \\ 0 \\ 1 \\ 0 \\ 0 \end{bmatrix} = \begin{bmatrix} c_{-2} \\ c_{-1} \\ c_0 \\ c_1 \\ c_2 \end{bmatrix} = \frac{2}{\pi}\begin{bmatrix} 0 \\ \exp\left(\frac{i\Delta\phi}{2}\right) \\ 0 \\ \exp\left(\frac{-i\Delta\phi}{2}\right) \\ 0 \end{bmatrix} \tag{3.9}$$

We see that both components in the output have powers $4/\pi^2 \approx 0.405$ and a phase difference of $\Delta\phi$.

3.2 Standard Resonator

In this section, we analyze the standard resonator, which does not implement beam recycling and spatial mode selection. We give matrices for the resonator elements, compute the round trip matrix, and find its eigenvalues and eigenvectors.

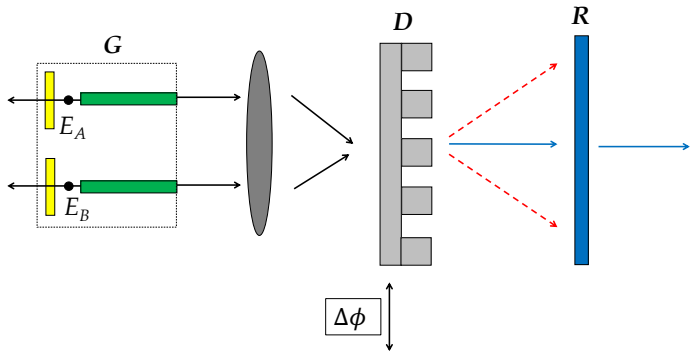

Figure 3.2: Model of the Dammann grating resonator. E_A and E_B denote the field amplitudes at the gain media end mirrors. $\Delta\phi$ is the induced phase error between the gain elements.

We begin by considering the field at the gain media end mirrors denoted by $\mathbf{E} = \begin{bmatrix} 0 & E_A & 0 & E_B & 0 \end{bmatrix}^T$. To form the resonator round trip matrix, we consider the elements of the resonator that act on this field as it propagates. These components are the gain media, the Dammann grating, and the resonator end mirror, shown in Figure 3.2.

The matrix $\mathbf{G}$ represents propagation of the field through the gain media and is given by

$$\mathbf{G} = \begin{bmatrix} 0 & 0 & 0 & 0 & 0 \\ 0 & g & 0 & 0 & 0 \\ 0 & 0 & 0 & 0 & 0 \\ 0 & 0 & 0 & g & 0 \\ 0 & 0 & 0 & 0 & 0 \end{bmatrix} \tag{3.10}$$

where g is the amplitude gain of both media. We assume the gain media have identical lengths so that no phase difference is acquired upon propagation.

After exiting the gain media, the field passes through the Dammann grating $\mathbf{D}$, given in Equation (3.8). Next, the distribution propagates to the resonator end mirror which applies optical feedback of amplitude reflectivity r to only the combined beam propagating along the optical axis. The matrix $\mathbf{R}$ represents the mirror and is given by

$$\mathbf{R} = r \begin{bmatrix} 0 & 0 & 0 & 0 & 0 \\ 0 & 0 & 0 & 0 & 0 \\ 0 & 0 & 1 & 0 & 0 \\ 0 & 0 & 0 & 0 & 0 \\ 0 & 0 & 0 & 0 & 0 \end{bmatrix} \tag{3.11}$$

Then, the field passes through the Dammann grating represented by $\mathbf{D^T}$. The transpose is necessary because the propagation angles are inverted due to reflection. Finally, the field again passes through the gain media. The round trip matrix is thus formed by the product of matrices

$$\mathbf{M_{RT}} = \mathbf{GD^TRDG} = \frac{4g^2 r}{\pi^2} \begin{bmatrix} 0 & 0 & 0 & 0 & 0 \\ 0 & m_1 & 0 & 1 & 0 \\ 0 & 0 & 0 & 0 & 0 \\ 0 & 1 & 0 & m_2 & 0 \\ 0 & 0 & 0 & 0 & 0 \end{bmatrix} \tag{3.12}$$

where $m_1 = \exp(-i\Delta\phi)$ and $m_2 = \exp(i\Delta\phi)$.

The eigenvalues and eigenvectors of the round trip matrix describe the supermodes of the resonator. They are found by solving the equation $\mathbf{M_{RT}E} = \lambda\mathbf{E}$. Since $\mathbf{M_{RT}}$ is rank 1 it has a single nonzero eigenvalue given by

$$\lambda = \frac{8g^2 r}{\pi^2} \cos(\Delta\phi) \tag{3.13}$$

with a corresponding eigenvector

$$\mathbf{E} = \begin{bmatrix} 0 \\ E_A \\ 0 \\ E_B \\ 0 \end{bmatrix} = \begin{bmatrix} 0 \\ 1 \\ 0 \\ e^{i\Delta\phi} \\ 0 \end{bmatrix} \tag{3.14}$$

The first step in describing the behavior of this supermode is to define the cold-cavity round trip power loss L as [46]

$$L = 1 - |\lambda|^2 = 1 - \frac{64r^2}{\pi^4} \cos^2(\Delta\phi) \tag{3.15}$$

where we set $g = 1$ in Equation (3.13). From this equation we see that the induced phase error $\Delta\phi$ changes the loss experienced by the supermode. The loss is unity for $\Delta\phi = \pi/2$ and $\Delta\phi = 3\pi/2$, meaning that after one round trip, the mode no longer exists in the resonator. The resonator does not allow oscillations at these values because it would require an infinite gain. The loss is minimized at $\Delta\phi = 0$ and $\Delta\phi = \pi$. This shows that the supermode loss is very susceptible to phase errors between the gain media.

In addition, we define the relative phase of the supermode as

$$\phi_{Rel} = \angle E_B - \angle E_A = \Delta\phi \tag{3.16}$$

where E_A and E_B are the eigenvector components given in Equation (3.14). This is simply the induced phase error. This suggests that the resonator cannot self-adjust in response to phase errors in the gain media.

Next, we compute the combined beam power as a function of induced phase error. To do this, we apply the Rigrod gain saturation model to the system and consider one of the two gain media, shown in Figure 3.3. This method was used to analyze a similar system with the Kramers-Kronig effect in [36]. The gain medium with small signal power gain is G_0 and saturated gain G is bounded by mirrors with reflectivities R_1 and R_2. The reflectivity R_1 represents the gain media end mirror and R_2 represents the effective reflectivity of the remainder of the beam combining resonator. P_1 and P_2 are the normalized powers incident on the mirrors R_1 and R_2. P_1 represents the power incident on the gain media end mirror and P_2 represents the power exiting the gain media into the free-space portion of the beam combining resonator.

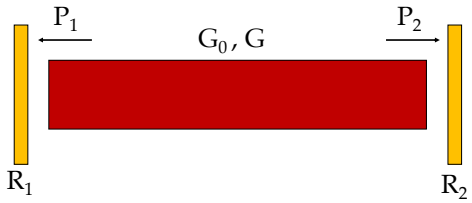

Figure 3.3: Model of the resonator used to apply gain saturation.

First, we compute the saturated gain during oscillation. We apply the steady-state condition $|\lambda| = 1$ to Equation (3.13) and solve for $G = g^2$ as a function of induced phase error.

$$G = g^2 = \frac{\pi^2}{8r\,|\cos\Delta\phi|} \tag{3.17}$$

From this equation, we see that the saturated power gain G changes as function of induced phase error $\Delta\phi$. Recall that increasing $\Delta\phi$ from zero causes an increase in the cavity loss. Since gain equals loss in steady-state, the saturated gain also increases. When the loss becomes so great that the saturated power gain equals the small signal gain of the medium G_0, the above equation becomes invalid since oscillations are suppressed. In particular, for $\Delta\phi = \frac{n\pi}{2}$ where n is an odd integer, G diverges to infinity, which is not physical.

Next, using the gain G, we can compute P_1. This can be expressed as

$$P_1 = \frac{P_2}{R_1 G} \tag{3.18}$$

We compute P_2 by quoting Equation (11) from the Rigrod analysis [47],

$$P_2 = \frac{\sqrt{R_1}\left(\ln G_0 + \ln\sqrt{R_1 R_2}\right)}{(\sqrt{R_1}+\sqrt{R_2})(1-\sqrt{R_1 R_2})} \tag{3.19}$$

Since R_2 is unknown, we eliminate it using the steady-state oscillation condition $R_1 R_2 G^2 = 1$,

$$P_2 = \frac{R_1 G^2 \ln\left(\frac{G_0}{G}\right)}{(1+R_1 G)(G-1)} \tag{3.20}$$

and after substitution into (3.18),

$$P_1 = \frac{P_2}{R_1 G} = \frac{G \ln\left(\frac{G_0}{G}\right)}{(1+R_1 G)(G-1)} \tag{3.21}$$

Finally, we multiply the eigenvector (3.14) by $\sqrt{P_1}$ from Equation (3.21) and propagate this vector through the gain media and Dammann grating to find the supermode vector in the external cavity $\mathbf{E_{cav}}$.

$$\mathbf{E_{cav}} = \begin{bmatrix} E_{U1} \\ 0 \\ E_C \\ 0 \\ E_{U2} \end{bmatrix} = \mathbf{DG}\sqrt{P_1}\mathbf{E} = \frac{2\sqrt{P_1 G}}{\pi} \begin{bmatrix} e^{\frac{i\Delta\phi}{2}} - \frac{1}{3}e^{\frac{5i\Delta\phi}{2}} \\ 0 \\ e^{\frac{-i\Delta\phi}{2}} + e^{\frac{3i\Delta\phi}{2}} \\ 0 \\ -\frac{1}{3}e^{\frac{-3i\Delta\phi}{2}} + e^{\frac{i\Delta\phi}{2}} \end{bmatrix} \tag{3.22}$$

where E_C represents the combined beam and $E_{U1,2}$ represent the two uncombined beams in the free-space section of the resonator.

The power in the combined beam is

$$P_C = |E_C|^2 = \frac{16}{\pi^2} P_1 G \cos^2(\Delta\phi) \tag{3.23}$$

P_C is plotted in Figure 3.4 using $r = 0.0481$, $G_0 = 19.5$ dB, and $R_1 = 0.04$. These parameters are used in the experimental system discussed in Chapter 4. P_C is normalized so that the maximum value is unity. The trend is roughly cosinusoidal, however, the laser is below threshold for $1.227\text{rad} < \Delta\phi < 1.868\text{rad}$ and $4.415\text{rad} < \Delta\phi < 5.006\text{rad}$

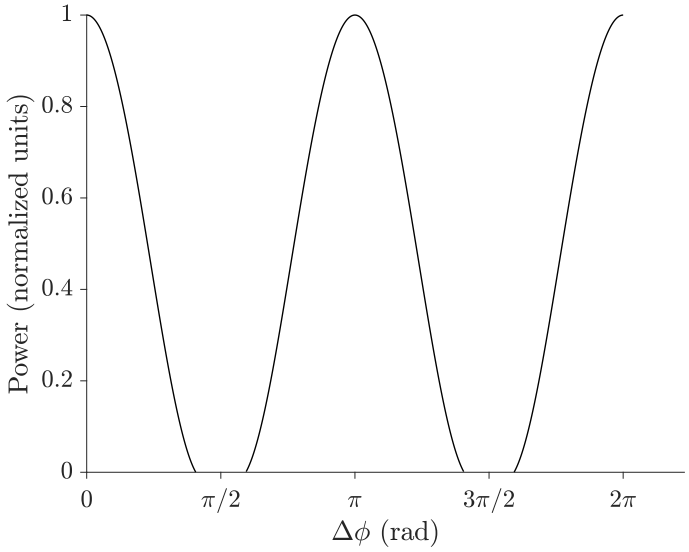

Figure 3.4: Theoretical combined beam power P_C for the standard resonator.

3.3 Recycling Resonator

In this section, we analyze the recycling resonator using the same methods developed in the previous section. This resonator implements beam recycling which causes spatial mode selection. We will demonstrate the resulting beneficial performance and also determine the particular condition that must be satisfied for it to occur.

The round trip matrix representing the recycling resonator is identical to Equation (3.12) except for the form of the matrix $\mathbf{R}$. This is because we apply feedback of

amplitude reflectivity r to the beams propagating at angles $\theta = \pm 2\lambda f_0$ in addition to the combined beam. The component propagating at $\theta = 2\lambda f_0$ will be reflected at an angle $\theta = -2\lambda f_0$ by the law of reflection. The modified reflectivity matrix takes the form

$$\mathbf{R} = r \begin{bmatrix} 0 & 0 & 0 & 0 & 1 \\ 0 & 0 & 0 & 0 & 0 \\ 0 & 0 & e^{i\phi_r} & 0 & 0 \\ 0 & 0 & 0 & 0 & 0 \\ 1 & 0 & 0 & 0 & 0 \end{bmatrix} \tag{3.24}$$

where we define the recycle phase shift ϕ_r as the phase shift between the on-axis and $\theta = \pm 2\lambda f_0$ components accrued from propagating through the resonator. For a general treatment of the recycling resonator and the associated matrices, see [43].

The particular value of ϕ_r has a significant impact on the resonator supermodes. First, we will show that any phase other than $\phi_r = 0$ and $\phi_r = \pi$ induces Kramers-Kronig (KK) self-phasing in the resonator. Recall that the KK effect occurs when there is a difference in the saturated gains of the gain elements [36]. This is the result of nonequal powers re-entering the gain media after feedback from the end mirror. Consider a field distribution with unity intensities exiting the gain media represented by $\mathbf{U} = \begin{bmatrix} 0 & 1 & 0 & 1 & 0 \end{bmatrix}^T$. We want to determine the intensities returning to the gain media as a function of ϕ_r. To do this, we compute $\mathbf{D^T R D U}$, which results in

$$\mathbf{D^T R D U} = \begin{bmatrix} 0 \\ U_A \\ 0 \\ U_B \\ 0 \end{bmatrix}$$

where

$$U_A = \frac{4r}{\pi^2}\left(\frac{10}{9} - \frac{2}{3}e^{-i\Delta\phi} + e^{i\phi_r}\left(1 + e^{-i\Delta\phi}\right)\right) \tag{3.25}$$

and

$$U_B = \frac{4r}{\pi^2}\left(\frac{10}{9} - \frac{2}{3}e^{i\Delta\phi} + e^{i\phi_r}\left(1 + e^{i\Delta\phi}\right)\right) \tag{3.26}$$

Now, using Equations (3.25) and (3.26), we find the difference in intensities returning

to the gain media,

$$I_A - I_B = |U_A|^2 - |U_B|^2 = \left(\frac{4r}{\pi^2}\right)^2 \frac{64}{9} \sin(\phi_r) \sin(\Delta\phi) \tag{3.27}$$

So, the field components are equal in intensity (for all phase errors $\Delta\phi$) only for $\phi_r = 0$ and $\phi_r = \pi$. This indicates that if beams of equal intensities exit the gain media and if the phase ϕ_r changes abruptly from 0 to, say, $\pi/2$ before the beams return to the gain media, one gain medium would receive more power and the KK effect would be induced in the system. To properly analyze this situation, the theory must be modified to include unequal gains and the KK phase as in [36]. We do not perform this analysis since it is beyond the scope of this work.

Next, we consider $\phi_r = \pi$ and determine the supermode losses versus induced phase errors. Substituting $\phi_r = \pi$ into Equation (3.24) and computing the round trip matrix gives

$$\mathbf{M_{RT}} = \mathbf{GD^T RDG} = \frac{4g^2 r}{3\pi^2} \begin{bmatrix} 0 & 0 & 0 & 0 & 0 \\ 0 & m_1 & 0 & \frac{1}{3} & 0 \\ 0 & 0 & 0 & 0 & 0 \\ 0 & \frac{1}{3} & 0 & m_2 & 0 \\ 0 & 0 & 0 & 0 & 0 \end{bmatrix} \tag{3.28}$$

where $m_1 = -5\exp(-i\Delta\phi)$ and $m_2 = -5\exp(i\Delta\phi)$. Solving for the eigenvalues results in

$$\lambda_{1,2} = \frac{4g^2 r}{\pi^2} \left(-\frac{5\cos(\Delta\phi)}{3} \pm \sqrt{\frac{25\cos^2(\Delta\phi)}{9} - \frac{224}{81}} \right) \tag{3.29}$$

where the subscript 1(2) indicates to take the $+(-)$ sign. In this equation, when $\cos^2(\Delta\phi) < \frac{224}{225}$, the term under the square root is negative. This means the magnitudes of the eigenvalues, and by extension the cold-cavity losses $L_{1,2} = 1 - |\lambda_{1,2}|^2$ shown in Figure 3.5, are identical for the two supermodes. As a result, oscillation in a single supermode cannot be achieved via gain clamping. The losses are distinct only for $-0.07\text{rad} < \Delta\phi < 0.07\text{rad}$. A similar interval exists centered on $\Delta\phi = \pi$. Single mode oscillation can occur in this narrow range, but may be difficult due to the very small difference in losses (0.003 at $\Delta\phi = 0$). In fact, this result is very similar to what was obtained for a spatially filtered cavity [48, 49]. So, this cavity implemented an equivalent type of beam recycling, but in a way that did not result in beneficial spatial mode selection.

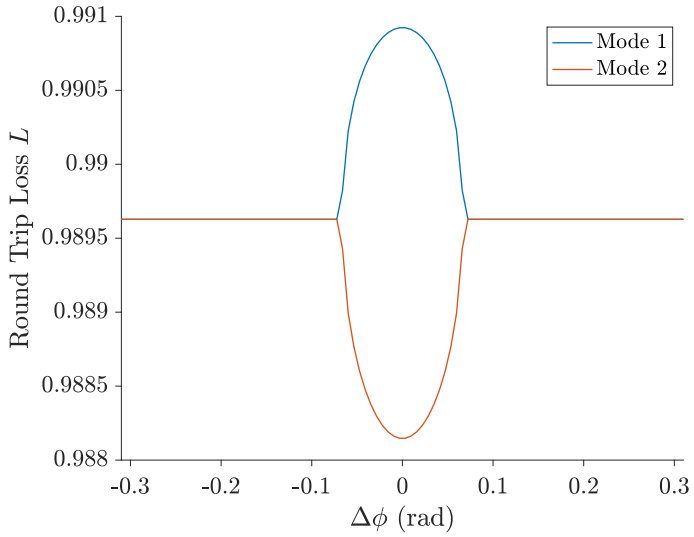

Figure 3.5: Supermode round trip power loss L versus induced phase error $\Delta\phi$ for the recycling resonator with $\phi_r = \pi$. The end mirror reflectivity is $r = 0.0481$.

Finally, we are left with the case $\phi_r = 0$. We now show this situation results in beneficial self-phasing due to spatial mode selection. Substituting $\phi_r = 0$ into Equation (3.24) above and computing the round trip matrix gives

$$\mathbf{M_{RT}} = \mathbf{G}\mathbf{D}^{\mathbf{T}}\mathbf{R}\mathbf{D}\mathbf{G} = \frac{4g^2 r}{3\pi^2}\begin{bmatrix} 0 & 0 & 0 & 0 & 0 \\ 0 & m_1 & 0 & \frac{19}{3} & 0 \\ 0 & 0 & 0 & 0 & 0 \\ 0 & \frac{19}{3} & 0 & m_2 & 0 \\ 0 & 0 & 0 & 0 & 0 \end{bmatrix} \tag{3.30}$$

where $m_1 = \exp(-i\Delta\phi)$ and $m_2 = \exp(i\Delta\phi)$. The eigenvalues are

$$\lambda_{1,2} = \frac{4g^2 r}{\pi^2}\left(\frac{\cos(\Delta\phi)}{3} \pm \sqrt{\frac{\cos^2(\Delta\phi)}{9} + \frac{352}{81}}\right) \tag{3.31}$$

with corresponding eigenvectors

$$\mathbf{E_{1,2}} = \begin{bmatrix} 0 \\ \frac{19}{9} \\ 0 \\ \frac{i\sin(\Delta\phi)}{3} \pm \sqrt{\frac{\cos^2(\Delta\phi)}{9} + \frac{352}{81}} \\ 0 \end{bmatrix} \tag{3.32}$$

where the subscript 1(2) indicates to take the $+(-)$ sign in the above equations.

The cold-cavity losses for these supermodes, defined as $L_{1,2} = 1 - |\lambda_{1,2}|^2$, are shown below in Figure 3.6 using an end mirror reflectivity of $r = 0.0481$. From the plot, we see that the losses are always less than unity. Since the losses are typically distinct from each other, gain clamping causes the resonator to select the lower-loss mode for oscillation. Recall that the standard resonator has unity loss for $\Delta\phi = \pi/2$ and $\Delta\phi = 3\pi/2$. In the recycling resonator, at $\Delta\phi = \pi/2$, the oscillating supermode switches from $\mathbf{E_1}$ to $\mathbf{E_2}$, and at $\Delta\phi = 3\pi/2$, it switches from $\mathbf{E_2}$ to $\mathbf{E_1}$. As a result, the loss of the oscillating mode never exceeds roughly 0.984. This demonstrates an improvement over the standard resonator since the oscillating supermode never experiences unity loss.

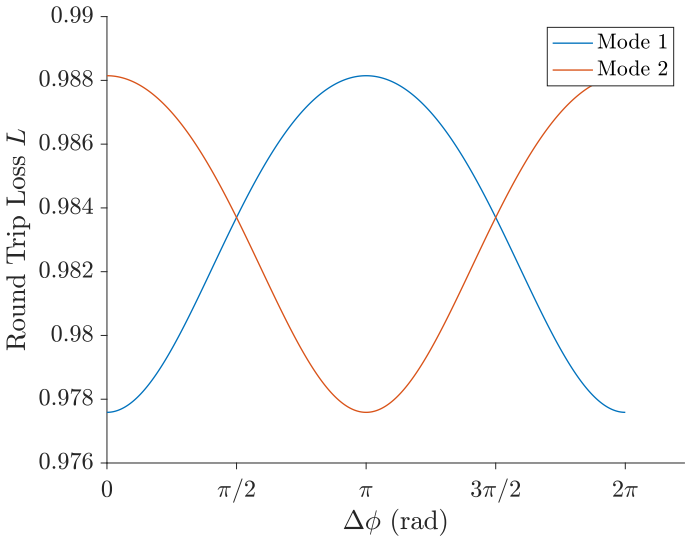

Figure 3.6: Supermode round trip power loss L versus induced phase error $\Delta\phi$ for the recycling resonator with $\phi_r = 0$. The end mirror reflectivity is $r = 0.0481$.

From Equation (3.32), the relative phases of the supermodes are

$$\phi_{Rel1,2} = \arctan\left(\frac{\pm\sin(\Delta\phi)}{\sqrt{\cos^2(\Delta\phi) + 352/9}}\right) \tag{3.33}$$

and are plotted in Figure 3.7. ϕ_{Rel1} shows oscillations versus phase error centered around 0 radians and ϕ_{Rel2} shows oscillations centered around π radians. The magnitude of the oscillations is roughly $\pi/20$ radians. Both supermodes exhibit significantly different phase behavior compared to the standard resonator.

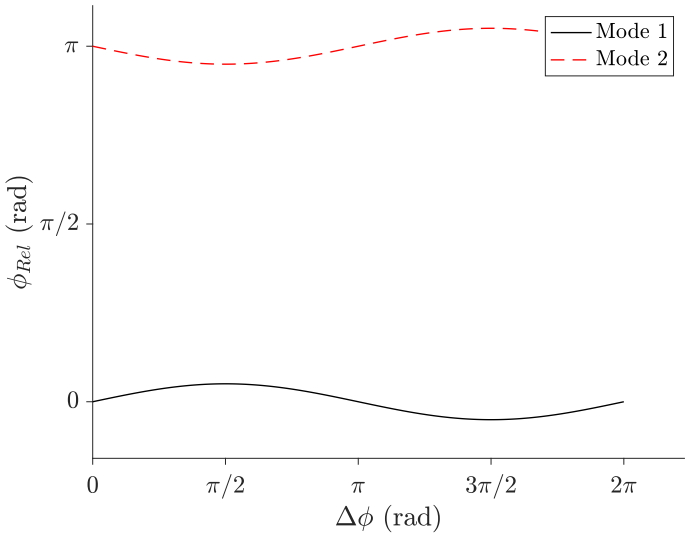

Figure 3.7: Supermode phases ϕ_{Rel1} and ϕ_{Rel2} versus induced phase error $\Delta\phi$ for the recycling resonator with $\phi_r = 0$.

The observed phase, taking into account the supermode losses, is shown in Figure 3.8. We also show the relative phase of the standard cavity supermode for comparison. To construct this trend, we plot ϕ_{Rel1} for the values of $\Delta\phi$ where $L_1 < L_2$ and plot ϕ_{Rel2} when $L_2 < L_1$. As $\Delta\phi$ increases from 0, the observed phase remains roughly constant. When the transition point at $\Delta\phi = \pi/2$ is reached, the phase jumps by roughly π radians. This shows that the oscillating mode is not very sensitive to additional phase errors, in contrast to the standard cavity. In particular, the supermode experiences about 1.41 rad of maximum passive phase adjustment, measured as the difference between the recycling and standard values of ϕ_{Rel} at $\Delta\phi = \pi/2$ and $\Delta\phi = 3\pi/2$. This is another benefit due to beam recycling and spatial mode selection.

Finally, we compute the combined beam power P_C using the same method discussed for the standard resonator. For a particular value of $\Delta\phi$, the saturated gain is determined from the eigenvalue of the lower-loss supermode. Then, the power at the gain media end mirrors is computed and the supermode eigenvector is propagated through the gain media and Dammann grating. The resulting trend is shown in Figure 3.9. The maximum output power versus phase error is normalized to unity. In contrast to the standard resonator, P_C remains above 0 for all phase errors. The power reaches its

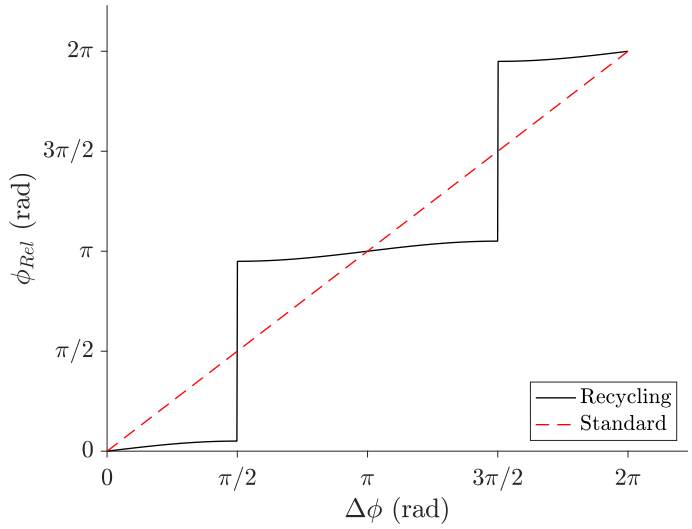

Figure 3.8: Observed supermode phase versus induced phase error $\Delta\phi$ for the recycling resonator with $\phi_r = 0$.

minimum at $\Delta\phi = \pi/2$ and $\Delta\phi = 3\pi/2$, which are the mode-transition points.

This discussion shows that beam recycling can result in enhanced laser performance due to spatial mode selection, but only for the particular recycle phase $\phi_r = 0$. In this case, the resonator exhibits less sensitivity to phase errors between the gain elements. The supermode phase and combined beam power do not change as drastically as in the standard resonator, and oscillation is supported for all phase errors. This represents improved resonator behavior arising from spatial mode selection. In the next chapter, we discuss an experimental setup implementing beam recycling and present data supporting the conclusions of the theory.

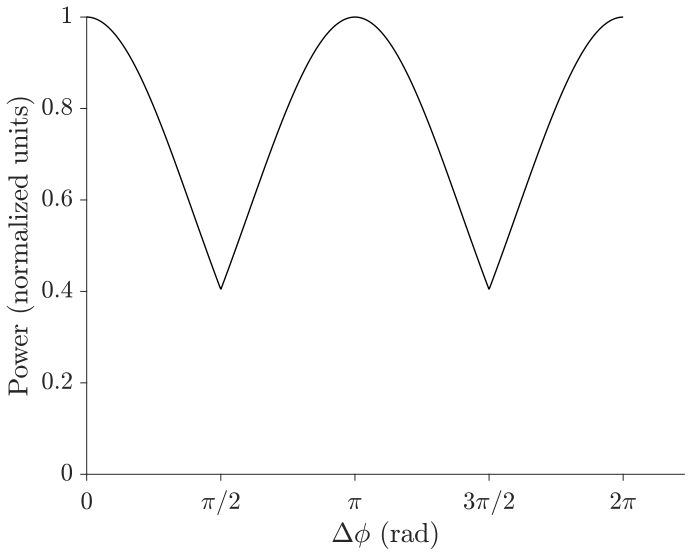

Figure 3.9: Combined beam power P_C versus induced phase error $\Delta\phi$ for the recycling resonator with $\phi_r = 0$.

Chapter 4

Experimental Demonstration in a Passively Coupled Fiber Laser

In the previous chapter, we discussed the analysis of a passive coherent beam combining resonator using a Dammann grating. In this chapter, we discuss an experimental implementation of the resonator using a two-core ytterbium-doped fiber for gain media. First, we discuss the experimental design including the fiber properties, resonator optics, and measurement techniques. Next, we show data for the supermode relative phase and combined beam power for the standard and recycling resonators for $\phi_r = 0$ and compare it to theory. We conclude the chapter by discussing the effects of nonzero recycle phase errors.

4.1 Experimental Design

In this section, we discuss the design of the laser resonator and the associated measurement systems. In addition, we discuss how self-phasing effects other than spatial mode selection are minimized. This experimental setup is very similar to one implemented in prior work [50, 51], including a study of Kramers-Kronig self phasing [36].

Figure 4.1 shows a diagram of the experimental setup. A 1-meter length of custom fabricated ytterbium-doped two-core fiber serves as the two gain media. The multimode inner cladding has a diameter of 150 microns and facilitates cladding pumping. An aspheric lens with 8mm focal length couples pump light into the inner cladding and

collimates light emitted by the fiber cores. The pump source is a 975nm diode laser emitting roughly 0.7 watts that is incident on the fiber cladding. A dichroic mirror (DM) transmits the pump light while reflecting the fiber's lasing wavelength to a measurement system to asses the laser supermode phase. The fiber cores have a diameter of 3.4 microns and a separation of 20 microns. This distance is large enough to avoid evanescent coupling between the cores. Two stress rods introduce high birefringence in the fiber cores, resulting in a polarization maintaining fiber. One end of the fiber is prepared with a 0° polish. This serves as the gain media end mirror with a 4% reflectivity arising from Fresnel reflections. The other end of the fiber is prepared using a 15° polish to suppress any back reflections from this facet. The fiber is coiled on a mandrel to minimize the optical path length (OPL) difference between the fiber cores [50]. Measurements with a probe laser show that the OPL difference is 57 microns.

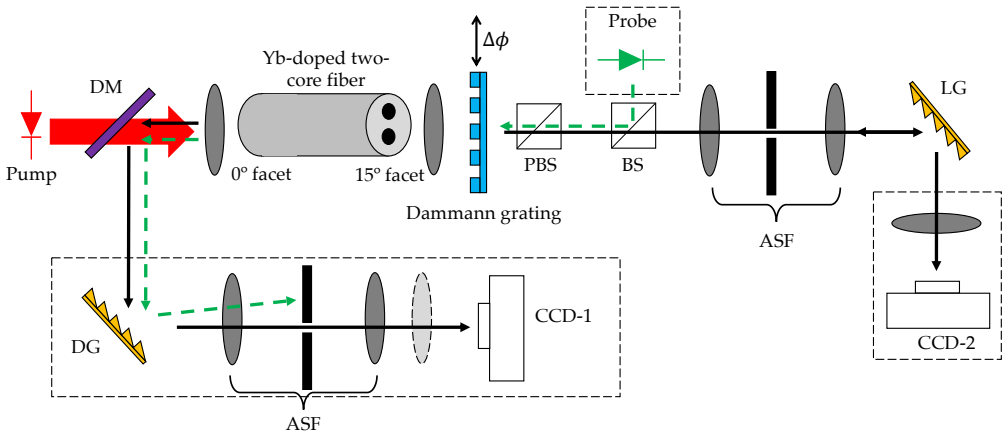

Figure 4.1: Diagram of experimental setup. Components inside dotted boxes are for measurement purposes.

An aspheric lens of focal length $f_1 = 11$ mm collimates light emitted by the 15° facet. This field passes through a Dammann grating. The period of the grating d is related to the lens focal length by $d = f_1\lambda/x$ where $x = 10$ microns is half of the distance between the fiber cores and $\lambda \approx 1$ micron. To achieve this, we use a grating with

period 1.44 mm placed at a 39° angle relative to the fiber axis. As a result, the phase depth of the grating is not π rad, which causes weak even harmonics to appear in the angular plane wave spectrum. These components do not have a significant impact on the laser behavior. The Dammann grating is mounted on a translation stage that allows phase errors to be induced between the fiber cores at a rate of 11.9 rad/mm determined from calibration. A polarizer (PBS) enforces lasing in a polarization state along one of the fiber's birefringent axes. An afocal system with a spatial filter (ASF) allows for selection of standard feedback or recycling feedback, as shown in Figure 4.2. The width of the spatial filter (slit) is adjusted with a micrometer. Finally, a blazed diffraction grating with 1200 lines/mm aligned at the Littrow angle (LG) applies optical feedback to the laser mode, coupling light back into fiber cores. The lasing wavelength is roughly 1063nm. We use a tunable, fiber-coupled diode laser to measure various properties of this system including the OPL difference, small signal gain, and cold-cavity loss. A beam splitter (BS) together with the Dammann grating couples this probe laser into the fiber cores. The probe power is sufficiently low to avoid saturation of the gain media.

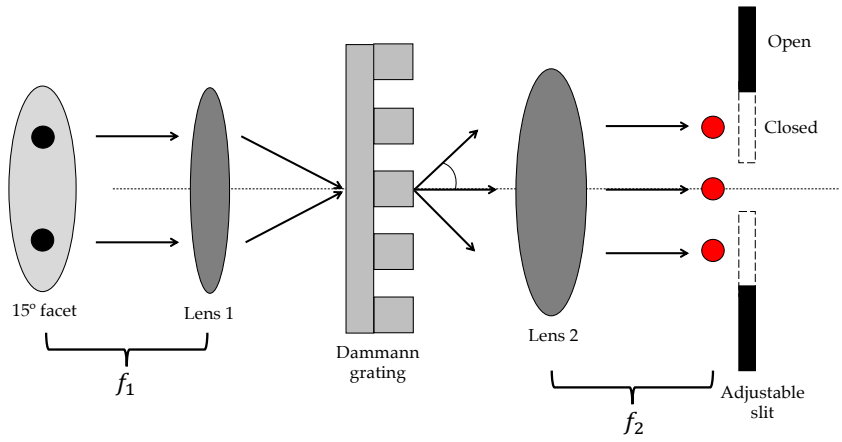

Figure 4.2: Illustration of spatial filtering inside resonator. The adjustable slit can either be closed (indicated by dotted lines) to form the standard resonator, or open to form the recycling resonator.

Measurement systems are shown inside dotted boxes in Figure 4.1. A diffraction

grating (DG) disperses output wavelengths from the 0° facet. A second afocal spatial filter (ASF) allows for measurement of either the oscillating supermode or the probe laser. In addition, the slit blocks residual pump light emitted by the fiber cladding and ASE from the fiber cores, reducing noise in the final signal. The result is an interference pattern that is formed in the plane of the camera CCD-1. A lens can be added between the afocal system and the camera to observe an image of the fiber cores. The phase of the interference pattern is determined by applying an FFT algorithm to the data recorded by the camera.

A second measurement system on the other end of the resonator measures the combined beam power. The Littrow grating produces a zeroth diffraction order (specular reflection) of the incident light. A lens forms the APWS of this distribution on a second camera CCD-2. The power is recorded by summing the intensity counts in the combined beam.

Several aspects of this design serve to minimize self-phasing mechanisms other than spatial mode selection. The 20 micron separation between the fiber cores means the cores are in the same thermal environment. As a result, fields propagating in the two cores will not experience phase shifts with respect to each other due to thermal changes in refractive index. The Kerr nonlinearity is made negligible by operating laser near threshold so that the circulating power does not exceed several milliwatts. Wavelength tuning is minimized using the combination of the small OPL difference in the fiber and the narrow lasing bandwidth enforced by the Littrow grating (LG). Wavelength tuning is less than 0.1nm in the experiment, which is equivalent to 0.03 rad of phase adjustment versus induced phase errors. The 15° facet's reflectivity is nearly -40 dB, which is sufficiently small to avoid regenerative feedback effects [40]. Finally, the KK effect is minimized by achieving near-equal coupling of components into fiber cores [36].

Several parameters were measured for this system in order to apply the gain saturation model. First, the passive fiber absorption found from a cutback measurement was 4.155 dB/m. The small signal gain at the operating pump power was $G_0 = 19.5$ dB. The cold-cavity loss was -14.1 dB, resulting in an effective end mirror reflectivity of $r = 0.0481$. Details of the techniques used to measure these quantities are discussed in Appendix A of [52].

4.2 Standard Resonator

To implement the standard resonator, the adjustable slit is closed to a size of roughly 400 microns. We measure the combined beam power and supermode relative phase at 10 micron steps of grating translation. To align the data and theory, the data is horizontally shifted by 1.4 rad since the true zero phase position of grating is not known.

The supermode relative phase is shown in Figure 4.3. Theory from Equation (3.16) is plotted alongside for comparison. Overall, the data shows a linear trend, agreeing with predictions. Near the phase error values representing high resonator loss, a small jump of about $\pi/5$ rad is seen in the phase data. This may be due to a residual KK effect between the fiber cores arising from alignment or mismatch between the core sizes. This suggests that while the KK effect can be minimized, the gain media always have some influence on self-phasing.

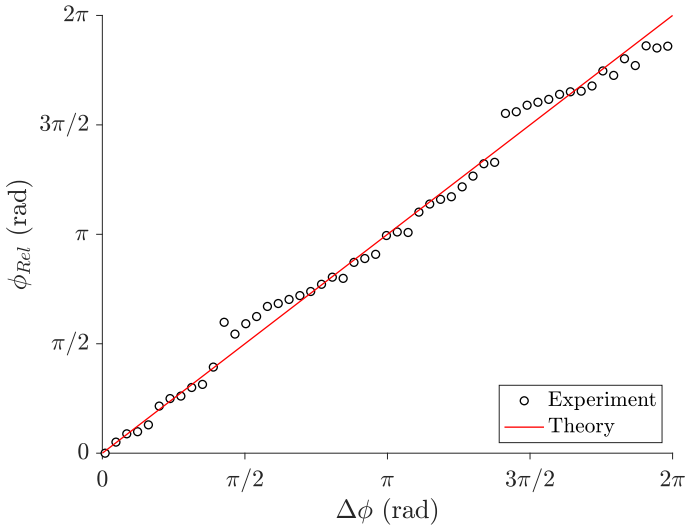

Figure 4.3: Measured and theoretical supermode relative phase ϕ_{Rel} for the standard resonator.

The combined beam power is shown in Figure 4.4. Near $\Delta\phi = \pi/2$ and $\Delta\phi = 3\pi/2$, when the supermode loss is unity, the raw data was slightly above zero due to ASE. We subtract this ASE value from all data points and normalize the maximum value of the power to unity. The average power versus phase error is 0.42. In addition, the observed power varies with time near the high-loss points, likely due to instabilities

occurring near threshold. Overall, these results also agree with theory and demonstrate an undesirable behavior. Oscillations from a system operating without any phase error can be suppressed from just a quarter-wave shift arising from technical noise. Resuming oscillation can result in Q-switching transients that not only affect the output power but could also damage the system due to a dramatic increase in power. These are situations that must be avoided in any practical system.

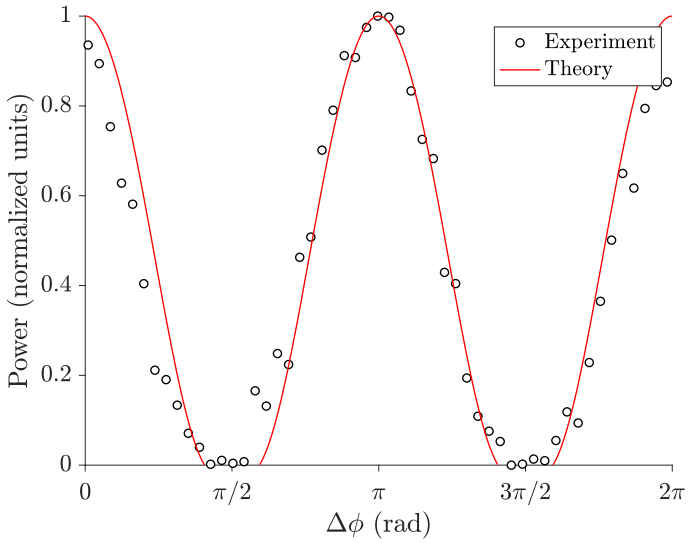

Figure 4.4: Measured and theoretical combined beam power P_C for the standard resonator.

4.3 Recycling Resonator

To implement the recycling resonator, the adjustable slit is opened to a size of roughly 1.2 mm. As before, we measure the combined beam power and supermode relative phase at 10 micron steps of grating translation. The data are horizontally shifted by 4.4 rad since the true zero phase position of grating is not known.

The supermode relative phase data is shown in Figure 4.5. The results show the distinct "staircase" shape predicted by theory, indicating that the supermodes show reduced sensitivity to phase errors compared to the standard resonator. The supermode fringe visibility is high throughout, indicating high coherence. The data indicates that

the resonator oscillates in one of two supermodes depending on the induced phase error.

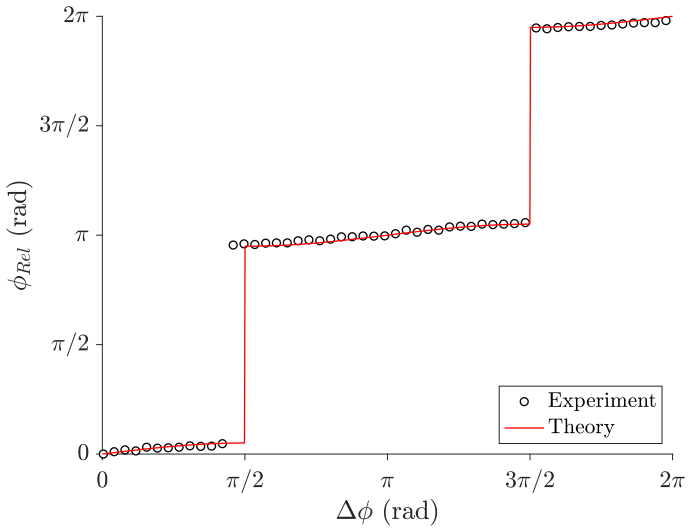

Figure 4.5: Measured and theoretical supermode relative phase ϕ_{Rel} for the recycling resonator.

The combined beam power is shown in Figure 4.6. We subtract the ASE value mentioned previously from all data points. The maximum value of the power is normalized to unity. The maximum output power of this system was roughly equal to that of the standard resonator. Here, the average power was 0.8, which is a 90% increase over the standard resonator. These results also show good agreement with theory. It is interesting to note that the data shows slightly better performance than theory since the power drops to 0.5 compared to 0.4 near $\Delta\phi = \pi/2$. Lasing is maintained for all induced phase errors. These results show a significant improvement over the standard resonator. A practical system implementing beam recycling that is subject to random phase errors from technical noise will be much less sensitive than a system without recycling.

We just showed that the beam recycling resonator leads to improved performance due to spatial mode selection. However, as discussed in Chapter 3, this benefit only occurs when the recycle phase shift $\phi_r = 0$. We conclude this chapter by showing experimental data for other values of ϕ_r. Experimental calibration gives 0.184 rad of recycle phase shift per centimeter of cavity length increase. First, we increase the cavity length by 10.5 cm, resulting in $\phi_r = 1.93$ rad and perform measurements in 20 micron

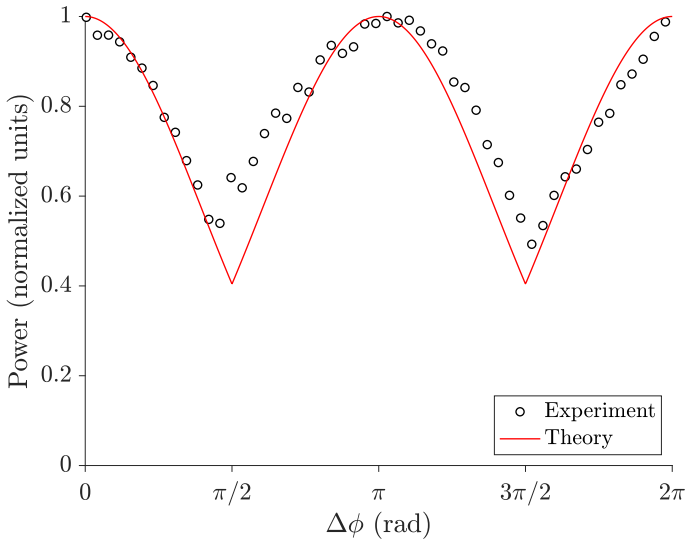

Figure 4.6: Measured and theoretical combined beam power P_C for the recycling resonator.

intervals. Recall that this phase shift results in unequal intensities coupling back into the gain media (see Equation (3.27)). This means that the saturated gains of the fiber cores are unequal and the KK effect is present in addition to spatial mode effects. The combined beam power is shown as black circles in Figure 4.7. The data is normalized such that unity represents the maximum output power from the previous two situations we considered. The power shows large variation versus the induced phase error, which is not desirable, with an average value of 0.25. The maximum output power is roughly 0.6, which is significantly less than that for the $\phi_r = 0$ case, which is 1. We have also computed the visibility $V = (I_{max} - I_{min})/(I_{max} + I_{min})$ of the supermode interference fringes and have plotted it as black circles in Figure 4.8. From this data, we see that the visibility decreases significantly near induced phase errors of $\pi/2$ and $3\pi/2$. In these regions, the system does not oscillate in a single supermode and the coherence of the array is reduced. Referring back to Figure 4.7, we see the combined beam power is low (between 0.1 and 0.2) when the visibility is high and vice versa. This means even when the array is coherent, the fields emitted by the fiber cores do not add in phase with each other at the Dammann grating and thus do not contribute power to the combined beam. These features are not desirable for a CBC system.

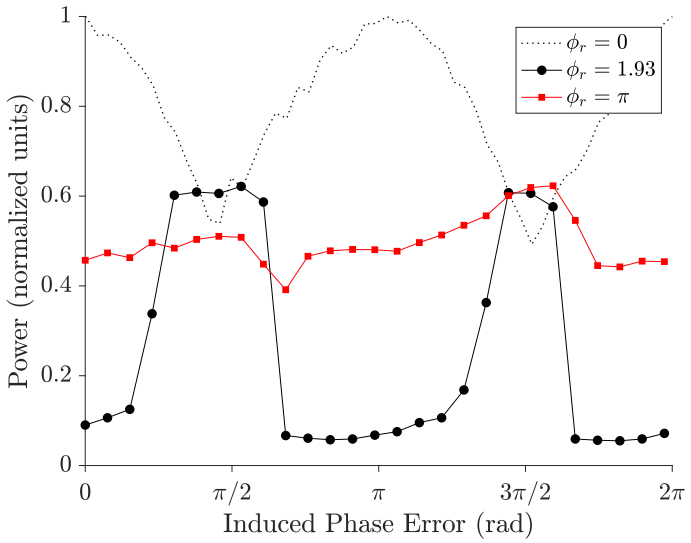

Figure 4.7: Measured combined beam power for recycle phase shifts of $\phi_r = 1.93$ and $\phi_r = \pi$. Power data for $\phi_r = 0$ is also shown for reference.

Finally, we present combined beam power and visibility data for $\phi_r = \pi$ as red squares in Figures 4.7 and 4.8. This phase shift was achieved by increasing the cavity length by 17 cm relative to the $\phi_r = 0$ position. The combined beam power, normalized in the same way as before, remains somewhat constant for all induced phase errors. The average power is 0.5. Compared to the $\phi_r = 1.93$ case, this seems like an improvement. However, the visibility data show the array has poor coherence for all phase errors. The minimum visibility is roughly 0.1 and the maximum is about 0.3, which is only slightly larger than the minimum visibility for $\phi_r = 1.93$. There are small increases in the coherence near induced phase errors of $\pi/2$ and $3\pi/2$, but it does not reach a high enough value to indicate oscillation in a single mode. In this scenario, coherent beam combining is not achieved since a single supermode with high-visibility fringes is not observed. In principle, this system can achieve single-supermode operation for a very small range of phase errors (see Equation (3.29), Figure 3.5, and the associated discussion). However, factors like a very small difference in supermode losses, gain effects, and insufficient control of phase errors could make this very difficult to achieve in practice. In any case, the behavior suggested by theory does not represent desirable behavior for a beam combining system. We have not shown supermode phase here since

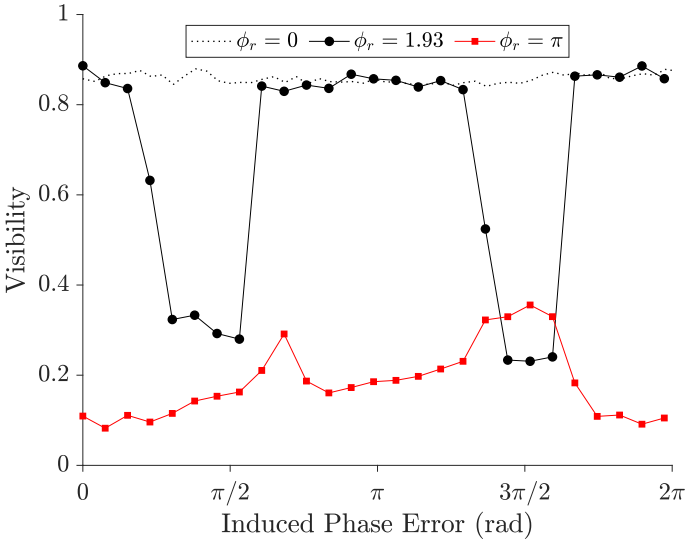

Figure 4.8: Measured supermode fringe visibility for recycle phase shifts of $\phi_r = 1.93$ and $\phi_r = \pi$. Visibility data for $\phi_r = 0$ is also shown for reference.

the phase is not well defined when the system exhibits poor coherence.

In conclusion, we have presented data illustrating beneficial self-phasing from spatial mode selection from a fiber CBC system. When $\phi_r = 0$, data from the standard and recycling resonators agree with theory. In addition, we have shown that other values of ϕ_r result in poor performance. As a whole, these experiments support the prediction that only one value of the recycle phase shift ϕ_r results in beneficial self-phasing from spatial mode selection. This conclusion appears to be significant for the design of a passive CBC system.

Chapter 5

Conclusion

In this thesis, we have studied spatial mode effects in a two-element passively coupled fiber laser. We began with a discussion of coherent beam combination (CBC) and the self-phasing effects that influence passive CBC systems. Next, we applied eigenmode analysis to a Dammann grating resonator and showed that beam recycling and spatial mode selection resulted in reduced sensitivity to phase errors between the gain elements. In particular, spatial mode selection causes the oscillating supermode phase and combined beam power to experience smaller changes versus phase errors compared to a resonator that does not implement the effect. We also determined the particular condition that must be satisfied for spatial mode selection to occur, namely, the recycle phase shift must be zero or an integer multiple of 2π. These results match the predictions made for a Michelson resonator [41].

Future work on this subject could move in several directions. One area of interest is how to shape the supermode losses versus induced phase error. Modes with small variations in loss may translate into small variations in combined beam power so long as there is sufficient discrimination between supermodes. In addition, experiments can be performed to determine the power scaling potential of beam recycling resonators when three or more gain elements are combined. Recent work has given some insight into this problem [43], but does not illustrate the properties of the individual supermodes of a system, leaving room for theoretical exploration. Finally, modeling and experiments can be performed to determine the behavior of systems under the influence of other self-phasing effects such as the Kerr nonlinearity and regenerative feedback.

References

[1] Fan, T. "Laser beam combining for high-power, high-radiance sources." *IEEE Journal of Selected Topics in Quantum Electronics*, *11*, 3: pp. 567–577, 2005.

[2] Augst, S.J.; Goyal, A.K.; Aggarwal, R.L.; Fan, T.Y.; and Sanchez, A. "Wavelength beam combining of ytterbium fiber lasers." *Opt. Lett.*, *28*, 5: pp. 331–333, Mar 2003.

[3] Sabourdy, D.; Kermene, V.; Desfarges-Berthelemot, A.; Vampouille, M.; and Barthelemy, A. "Coherent combining of two nd:yag lasers in a vernier-michelson-type cavity." *Applied Physics B Lasers and Optics*, *75*: pp. 503–507, Oct 2002.

[4] Leger, J.R.; Swanson, G.J.; and Veldkamp, W.B. "Coherent laser addition using binary phase gratings." *Applied optics*, *26*, 20, 1987.

[5] Leger, J.R. "Lateral mode control of an algaas laser array in a talbot cavity." *Applied Physics Letters*, *55*, 4: pp. 334–336, 1989.

[6] Rediker, R.H.; Schloss, R.P.; and Van Ruyven, L.J. "Operation of individual diode lasers as a coherent ensemble controlled by a spatial filter within an external cavity." *Applied Physics Letters*, *46*, 2: pp. 133–135, 1985.

[7] Kapon, E.; Katz, J.; and Yariv, A. "Supermode analysis of phase-locked arrays of semiconductor lasers." *Opt. Lett.*, *9*, 4: pp. 125–127, Apr 1984.

[8] Anderegg, J.; Brosnan, S.; Cheung, E.; Epp, P.; Hammons, D.; Komine, H.; Weber, M.; and Wickham, M. "Coherently coupled high-power fiber arrays." In "Proc. SPIE," vol. 6102, 2006.

[9] Cheung, E.C.; Ho, J.G.; Goodno, G.D.; Rice, R.R.; Rothenberg, J.; Thielen, P.; Weber, M.; and Wickham, M. "Diffractive-optics-based beam combination of a phase-locked fiber laser array." *Opt. Lett.*, *33*, 4: pp. 354–356, Feb 2008.

[10] Shay, T.M. "Theory of electronically phased coherent beam combination without a reference beam." *Opt. Express*, *14*, 25: pp. 12188–12195, Dec 2006.

[11] Shay, T.M.; Benham, V.; Baker, J.T.; Sanchez, A.D.; Pilkington, D.; and Lu, C.A. "Self-synchronous and self-referenced coherent beam combination for large optical arrays." *IEEE Journal of Selected Topics in Quantum Electronics*, *13*, 3: pp. 480–486, May 2007.

[12] Zhou, P.; Liu, Z.; Wang, X.; Ma, Y.; Ma, H.; Xu, X.; and Guo, S. "Coherent beam combining of fiber amplifiers using stochastic parallel gradient descent algorithm and its application." *IEEE Journal of Selected Topics in Quantum Electronics*, *15*, 2: pp. 248–256, March 2009.

[13] Vorontsov, M.A. and Sivokon, V.P. "Stochastic parallel-gradient-descent technique for high-resolution wave-front phase-distortion correction." *J. Opt. Soc. Am. A*, *15*, 10: pp. 2745–2758, Oct 1998.

[14] Yu, C.X.; Augst, S.J.; Redmond, S.M.; Goldizen, K.C.; Murphy, D.V.; Sanchez, A.; and Fan, T.Y. "Coherent combining of a 4 kw, eight-element fiber amplifier array." *Opt. Lett.*, *36*, 14: pp. 2686–2688, Jul 2011.

[15] Richardson, D.J.; Nilsson, J.; and Clarkson, W.A. "High power fiber lasers: current status and future perspectives (invited)." *J. Opt. Soc. Am. B*, *27*, 11: pp. B63–B92, Nov 2010.

[16] Jeux, F.; Desfarges-Berthelemot, A.; Kermène, V.; and Barthelemy, A. "Efficient passive phasing of an array of 20 ring fiber lasers." *Laser Physics Letters*, *11*, 9: p. 095003, Jul 2014.

[17] Wu, T.W.; Chang, W.Z.; Galvanauskas, A.; and Winful, H.G. "Dynamical, bidirectional model for coherent beam combining in passive fiber laser arrays." *Opt. Express*, *18*, 25: pp. 25873–25886, Dec 2010.

[18] Guillot, J.; Desfarges-Berthelemot, A.; Kermène, V.; and Barthélémy, A. "Experimental study of cophasing dynamics in passive coherent combining of fiber lasers." *Opt. Lett.*, *36*, 15: pp. 2907–2909, Aug 2011.

[19] Fridman, M.; Eckhouse, V.; Davidson, N.; and Friesem, A.A. "Effect of quantum noise on coupled laser oscillators." *Phys. Rev. A*, *77*: p. 061803, Jun 2008.

[20] Sabourdy, D.; Desfarges-Berthelemot, A.; Kermene, V.; and Barthelemy, A. "Coherent combining of q-switched fibre lasers." *Electronics Letters*, *40*, 20: pp. 1254–1255, Sep. 2004.

[21] Klenke, A.; Seise, E.; Demmler, S.; Rothhardt, J.; Breitkopf, S.; Limpert, J.; and Tünnermann, A. "Coherently-combined two channel femtosecond fiber cpa system producing 3 mj pulse energy." *Opt. Express*, *19*, 24: pp. 24280–24285, Nov 2011.

[22] Kouznetsov, D.; Bisson, J.F.; Shirakawa, A.; and Ueda, K.i. "Limits of coherent addition of lasers: Simple estimate." *Optical Review*, *12*, 6: pp. 445–447, Nov 2005.

[23] Rothenberg, J.E. "Passive coherent phasing of fiber laser arrays." In "Proc. SPIE," vol. 6873, 2008.

[24] Siegman, A.E. "Resonant modes of linearly coupled multiple fiber laser structures." *Unpublished*, pp. 1–25, 2004.

[25] Brown, D.C. and Hoffman, H.J. "Thermal, stress, and thermo-optic effects in high average power double-clad silica fiber lasers." *IEEE Journal of Quantum Electronics*, *37*, 2: pp. 207–217, Feb 2001.

[26] Jansen, F.; Stutzki, F.; Otto, H.J.; Eidam, T.; Liem, A.; Jauregui, C.; Limpert, J.; and Tünnermann, A. "Thermally induced waveguide changes in active fibers." *Opt. Express*, *20*, 4: pp. 3997–4008, Feb 2012.

[27] Davis, M.K.; Digonnet, M.J.F.; and Pantell, R.H. "Thermal effects in doped fibers." *Journal of Lightwave Technology*, *16*, 6: pp. 1013–1023, June 1998.

[28] Augst, S.J.; Fan, T.Y.; and Sanchez, A. "Coherent beam combining and phase noise measurements of ytterbium fiber amplifiers." *Optics letters*, *29*, 5, 2004.

[29] Agrawal, G. *Nonlinear Fiber Optics*. Academic Press, fifth ed., 2013.

[30] Bochove, E.J.; Cheo, P.K.; and King, G.G. "Self-organization in a multicore fiber laser array." *Opt. Lett.*, *28*, 14: pp. 1200–1202, Jul 2003.

[31] Bochove, E.J.; Zunoubi, M.R.; and Corcoran, C.J. "Effect of kerr and resonant nonlinearities on phase locking of a multistable fiber amplifier array." *Opt. Lett.*, *38*, 23: pp. 5016–5019, Dec 2013.

[32] Bochove, E.J.; Aceves, A.B.; Braiman, Y.; Colet, P.; Deiterding, R.; Jacobo, A.; Miller, C.A.; Rhodes, C.; and Shakir, S.A. "Model of the self-q-switching instability of passively phased fiber laser arrays." *IEEE Journal of Quantum Electronics*, *47*, 6: pp. 777–785, June 2011.

[33] Fotiadi, A.A.; Antipov, O.L.; and Mégret, P. "Dynamics of pump-induced refractive index changes in single-mode yb-doped optical fibers." *Opt. Express*, *16*, 17: pp. 12658–12663, Aug 2008.

[34] Henry, C. "Theory of the linewidth of semiconductor lasers." *IEEE Journal of Quantum Electronics*, *18*, 2: pp. 259–264, February 1982.

[35] Arkwright, J.W.; Elango, P.; Atkins, G.R.; Whitbread, T.; and Digonnet, J.F. "Experimental and theoretical analysis of the resonant nonlinearity in ytterbium-doped fiber." *Journal of Lightwave Technology*, *16*, 5: pp. 798–806, May 1998.

[36] Kunkel, W.M. and Leger, J.R. "Gain dependent self-phasing in a two-core coherently combined fiber laser." *Optics express*, *26*, 8, 2018.

[37] Kunkel, W.M. and Leger, J.R. "Kramers-kronig self-phasing effect in passive beam combining resonators." In "Proc. SPIE," vol. 10904, p. 109041N, 2019.

[38] Kunkel, W.M.; Chiang, H.S.; and Leger, J.R. "Bistable operation of a two-core coherently combined fiber laser." In "Laser Congress 2017 (ASSL, LAC)," p. JM5A.29. Optical Society of America, 2017.

[39] Corcoran, C.J. and Durville, F. "Passive phasing in a coherent laser array." *IEEE Journal of Selected Topics in Quantum Electronics*, *15*, 2: pp. 294–300, March 2009.

[40] Corcoran, C.J.; Durville, F.; and Ray, W. "Regenerative phase shift and its effect on coherent laser arrays." *IEEE Journal of Quantum Electronics*, *47*, 7: pp. 1043–1048, July 2011.

[41] Khajavikhan, M. and Leger, J. "Modal analysis of path length sensitivity in superposition architectures for coherent laser beam combining." *IEEE Journal of Selected Topics in Quantum Electronics*, *15*, 2: pp. 281–290, 2009.

[42] Khajavikhan, M.; John, K.; and Leger, J.R. "Experimental measurements of supermodes in superposition architectures for coherent laser beam combining." *IEEE Journal of Quantum Electronics*, *46*, 8: pp. 1221–1231, 2010.

[43] Kunkel, W.M. and Leger, J.R. "Passive coherent laser beam combining with spatial mode selecting feedback." *IEEE Journal of Quantum Electronics*, *55*, 4: pp. 1–8, Aug 2019.

[44] Dammann, H. and Klotz, E. "Coherent optical generation and inspection of two-dimensional periodic structures." *Optica Acta: International Journal of Optics*, *24*, 4: pp. 505–515, 1977.

[45] Goodman, J.W. *Introduction to Fourier Optics*. Roberts & Company, third ed., 2005.

[46] Siegman, A.E. *Lasers*. University Science Books, 1986. Pg. 567.

[47] Rigrod, W.W. "Saturation effects in high-gain lasers." *Journal of Applied Physics*, *36*, 8: pp. 2487–2490, 1965.

[48] Wan, C.; Tiffany, B.; and Leger, J.R. "Analysis of path length sensitivity in coherent beam combining by spatial filtering." *IEEE Journal of Quantum Electronics*, *47*, 6: pp. 770–776, 2011.

[49] Wan, C. and Leger, J.R. "Experimental measurements of path length sensitivity in coherent beam combining by spatial filtering." *IEEE Journal of Quantum Electronics*, *48*, 8: pp. 1045–1051, 2012.

[50] Chiang, H.S.; Leger, J.R.; Nilsson, J.; and Sahu, J. "Direct observation of kramers-kronig self-phasing in coherently combined fiber lasers." *Optics letters*, *38*, 20, 2013.

[51] Chiang, H.S.; Nilsson, J.; Sahu, J.; and Leger, J.R. "Experimental measurements of the origin of self-phasing in passively coupled fiber lasers." *Optics letters*, *40*, 6, 2015.

[52] Kunkel, W.M. *Passive coherent beam combining by gain effects in fiber lasers and spatial beam control in gradient refractive index media.* Ph.D. thesis, University of Minnesota, 2018.